Enabling cryogenic gravitational wave detectors: growth of sapphire crystals with record low absorption in the near infrared

T Aventin, A. Nehari, Danièle Forest, J. Degallaix, C. Dujardin, Gianpietro Cagnoli, Kheirreddine Lebbou

Enabling cryogenic Gravitational Waves detectors: growth of sapphire crystals with record low absorption in the near infrared

T. Aventin[1], A. Nehari[1], D. Forest[2], J. Degallaix[2], C.Dujardin[1], G.Cagnoli[1], K. Lebbou[1]

[1]Institut Lumière Matière (ILM), UMR 5306 Université Lyon1-CNRS, Université de Lyon, Lyon 69622, Villeurbanne Cedex, France

[2]LMA – CNRS/IN2P3 Laboratoire des Matériaux Avancés, 69100 Villeurbanne, France

Abstract

15 ultra-pure sapphire single crystals of diameter 32 mm and 100 mm long were grown under stationary stable regime using Czochralski (Cz) technique. Despite varying several growth parameters, the obtained crystals were transparent without visible macroscopic defects such as cracks, inclusions and grains boundaries. The optical absorption coefficients (α) at the 1064 nm wavelength of the grown sapphire crystals were mapped by the Photothermal Deflection Spectroscopy (PDS). C-axis crystals grown using low pulling rates of 1.5 mm/h and lower present very low 1064nm optical absorption coefficients of α=11 ppm/cm. At such low levels the origin of the optical absorption has never been explained. However, in this paper we point toward the role of Fe^{2+}- Fe^{3+} and Ti^{3+}- Ti^{3+} pairs.
These results open the route to upscaling the growth process to achieve ultra-large sapphire crystals with outstanding optical performances, which are a key for the next generation of gravitational wave detectors.

Keywords: Sapphire, Growth, PDS, Absorption, Defects, 1064nm

1. Introduction

With the first direct gravitational wave (GW) detection in 2015 [1], the Universe has started to be explored by a completely new messenger. After exploiting all bands of the electromagnetic spectrum, GW detection opened a new window on the Universe, enabling the regular study of extragalactic objects.

Space-time deformations produced by the gravitational waves are measured by monitoring the position of mirrors suspended in a Michelson interferometer configuration, whose sensitivity to mirror displacements is enhanced by the use of km long Fabry-Perot cavities in each arm [2]. All the signals detected so far came from the merger of compact objects such as black holes (BH) or neutron stars (NS). Signals from supernovae (SN), pulsars and more exotic phenomena such as the cosmic string or the cosmic microwave background [3] have yet to be detected. Such phenomenon need a controlled technology and performed materials.

Among materials, sapphire is a unique material combining excellent mechanical properties with exceptional optical performance [4-6]. It is the second hardest material after diamond and it has a very wide optical transmission band ranging from UV ($\lambda \approx 200$ nm) to midinfrared ($\lambda \approx 5$ µm) [7-9]. It also has excellent thermal properties with a very high congruent melting point of 2050 °C and a very high thermal conductivity [10-11]. It is therefore naturally used in a wide range of cutting-edge applications ranging from military applications to extreme physics experiments such as gravitational wave detection [12-14].

Reaching the true cosmological distances of future cryogenic GW detectors is only possible if a crystalline material with sufficiently low absorption is available in large dimensions. For cryogenic operation, the material must be monocrystalline, as all amorphous materials, such as the fused silica used in all room-temperature detectors, have far too high thermal noise levels [15]. There are two promising crystalline materials. Silicon, which can be produced by directional solidification in large dimensions required by the GW detector (50 cm diameter) [16], has an absorption of several hundred ppm/cm. Sapphire, currently used for the Japanese gravitational wave detector KAGRA 22 cm diameter mirrors, has an average absorption of 50 ppm/cm [17]. Neither of these materials is compatible with the European Einstein Telescope (ET) requirements.

While promising on paper, some problems with the use of sapphire substrates have been highlighted, most notably its optical absorption at 1064 nm. A higher optical absorption means reducing the laser power to avoid introducing excess heat than can't be extracted from the mirrors while maintaining the mirror nominal temperature. However, a lower laser power increases the quantum noise, leading to an overall reduction in the detector sensitivity. Unexpected birefringence, despite using c-axis sapphires has also been measured.

This low absorption sapphire removes the main obstacle for any GW cryogenic detector. For ET, it means being able to have 5 times more laser power and, consequently, $\sqrt{5}$ times less quantum noise at 30 Hz. Birefringence effects degrade the sensitivity of gravitational wave detectors, not only because they introduce optical losses, but also because it's spatial fluctuations create extra phase noise in the arm cavity reflected beam [18]. As sapphire is a birefringent material with its optical axis along the c-axis, substrates for the GW detector mirrors must be aligned along the c-axis.

In this work, we report the czochralski growth of 3.5 cm-diameter sapphire single crystals that exhibit a record absorption of 10ppm/cm in a controlled and repeated manner and to investigate the origin of this absorption.

2. Experimental section

2.1 Crystal growth

Under stationary stable growth regime, 15 sapphire bulk–single crystals were grown by Czochralski technique, using the same oven in argon atmosphere [19-21]. To ensure that the melting temperature crystal growth is maintained, the control program freely controls the generator heating power output. Two oriented seed were used for pulling crystals from the melt, one for the c-axis and another one for the a-axis.

The raw materials used were high purity sapphire crackles grown by RSA le Rubis company [22] using the Verneuil growth method. Glow discharge mass spectroscopy (GDMS) analysis of the feed material used in the experiments is shown in Table 1. It can be seen that most elements are close to their detection limit for the analysis and confirm the high purity of the used starting raw material.

Table 1. Impurity Analyses of Alumina Raw Material Using Glow Discharge Mass Spectroscopy (GDMS, ppm wt)

Fe	Cr	Ti	Co	Ni	Mn	V	Ir	Na	Si	P	Cl	K	Ga
1.7	0.28	0.75	0.08	<0.05	<0.05	<0.05	<0.1	12.5	2.4	1.2	1.5	2.3	2.7

2.2 Optical absorption measurement

The 1064 nm absorption coefficient mappings of the sapphire samples were measured using the Photo-Deflection Spectroscopy (PDS) technique [24], **figure 1a**. This method uses the mirage effect to obtain a precise measurement of the absorption coefficient α inside the volume of a transparent material. A high power laser at 1064 nm is focused inside the substrate, where a very small amount of the light is absorbed (**figure 1b**). The absorbed light is converted to heat creating a gradient of temperature inside the sample. A second laser, at a different wavelength is deflected by this gradient. The absorption coefficient is directly proportional to the deflection of this probe laser recorded by a quadrant detector.

Since the tested samples are mounted on transverse displacement stages, it is possible to do a 2D mapping of the absorption. For this paper, a mapping on a diameter of 30 mm on each sample has been done with a lateral step size of 2 mm. To study the absorption along the crystal growth direction each crystal has been cut in 3 or 4 pieces along the growth axis. As can be seen on **figure 1b,** the signal detected by the quadrant detector is then read by a lock-in amplifier. This is because the pointing instability of the probe beam (or beam jitter) is a major noise source of this technique at low frequency. In order to mitigate the impact of this noise, the pump beam intensity is modulated at a high frequency. The lock-in amplifier then extracts the signal from the quadrant detector at the given modulation frequency.

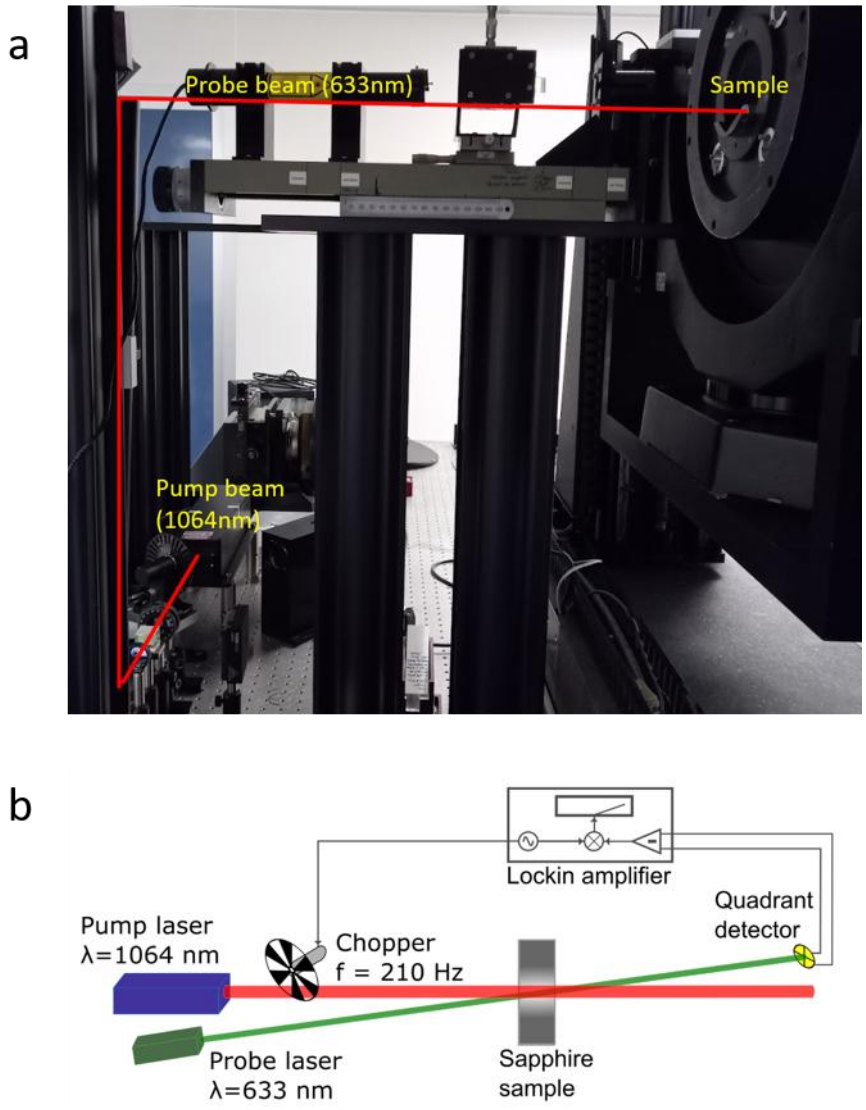

Figure 1. Picture of the PDS bench (1a) and schematic diagram of a collinear 1064nm PDS bench (1b).

3. Results and discussion

3.1 Czochralski sapphire crystals grown from the melt

The cylindrical shaped crystals were grown with a total length of 100 mm and a diameter of 35 mm. The experimental apparatus allowed for a control of the different growth parameters, and in particular the pulling and rotation rate, the rod rotation speed (the speed at which the rod that holds the crystal turns) and the crucible counter rotation speed (the speed at which the whole structure turns, in the opposite direction to the seed).

The rotation speed is an important parameter for two reasons. The first one is that it allows obtaining the desired circular cross section. Without any rotation, the crystal will grow faster along a specific direction corresponding to minimum heat transport from the melt to the crystal. If the machine does not have perfect thermal symmetry along the vertical axis

coincident with the growth directions, the crystal would wander off the pulling axis producing an object with spiral shape and without any symmetry and strong variations in diameter (**figure 2**). The second one concerns the distribution of the unwanted impurities coming from the initial raw materials. Without any rotation the impurities in the melt would be subject to the effect of the natural convective flow in the melt. This flow is driven principally by the buoyancy created by the temperature field. Finally, the crucible rotation also affects the geometry of the crystal-melt interface, an important factor in controlling crystal perfection.

All the crystals grown were then cut into 15 mm thick cylinders, 30 mm in diameter and polished on both sides to obtain a transparent sample. Photos of the as grown sapphire crystals, as well as samples cut and polished from the crystals are presented in **figure 3.** The grown crystal presents a high macroscopic surface quality, controlled shape and they witness of an accurate control throughout the crystal growth process. They are macroscopically defects free. The crystals grown along a-axis presented two facets and along the c-axis, they present hexagonal shape with six facets. The most observed defects in Czochralski crystal growth technology are gaseous, solid inclusions and grains boundaries [23]. The reason of such defects origin is crystal super-cooling and hence loss of the crystallization stability front. In order to overcome these problems and to control the growth conditions at the crystallization interface and prevent the formation of related defects, an automatic control system using a crystal weight sensor was applied to the process. The growth parameters used for each crystal are summarized in **table 2** and the average absorption (discussed later) has been added. We did GDMS analysis on three samples (**table 3**). When looking at the first seven elements, we can see that the concentrations for cobalt, nickel, manganese and vanadium are very low, below 0.1 ppm for these 4 elements (with the exception of nickel in sample 193). There is however between a few and a few tenths of ppm of iron, chromium and titanium in all three of these samples. The phosphorus concentration goes from 3.6ppm in 191 to less than 0.005ppm in 196 or chlorine with 191 displaying 16ppm and 193 and 196 having 0.52 and 0.07ppm respectively.

Figure 2: Sapphire ingot grown without automatic program showing diameter instability.

Figure 3: Top: picture of the sapphire crystals grown under stationary stable regime. Bottom: different samples of 15 mm thick cylinder prepared from sapphire ingot

Table 2: Summary tables of the all the sapphire crystal grown.

Crystal reference	**Crystal orientation**	**Pulling rate (mm/h)**	**Rod rotation speed (rpm)**	**Crucible rotation Speed (rpm)**	**Mean α at 1064nm (ppm/cm)**
191	A	2	4	0	56
192	C	2	4	0	44
193	C	2	8	0	38
194	C	2	16	0	33
196	C	1.5	4	0	17
197	C	2	4	1	18
198	C	2	12	1	24
199	C	2	12	0	22
204	A	2	8	0	44
205	C	2	4	0	15
206	C	1.5	12	0	11
207	C	1	4	0	11
212	C	1	6	0	10
213	C	1	4	1	20
214	A	1	4	1	44

Table 3: GMDS analysis results on samples taken from the tail of crystals 191, 193 and 196. Concentrations are given in ppm of total weight

Chemical elements	191 (ppm)	193(ppm)	196(ppm)
Fe	2.8	3.7	1.5
Cr	0.37	1.3	0.42
Ti	0.85	0.66	0.91
Co	0.07	<0.05	<0.05
Ni	<0.05	0.26	0.06
Mn	<0.05	0.08	<0.05
V	<0.05	<0.05	<0.05
Ir	<0.1	<0.1	5.2
Na	15	6.9	11
Si	5.8	1.3	2.3
P	3.6	0.26	<0.005
Cl	16	0.52	0.07
K	<0.5	5.3	0.07
Ga	3.6	0.35	3.2

3.2 Mean absorption

Table 2 presents the growth parameters and the crystals mean absorption coefficients of 15 samples cut from sapphire crystals samples. The numbers attributed to each crystal are related to the order in which they were produced, 191 being the first and 214 being the last. The mean absorption coefficients of the crystals were calculated by averaging the mean absorption coefficient (α) of each sample from the same crystal.

We obtain very low absorption coefficients for all our crystals, ranging from 56 ppm/cm (191) for the highest to 10 ppm/cm for the lowest (212). Although these results are achieved on much smaller crystals than the ones used as test masses in KAGRA (220 mm in diameter and 150 mm thick), this is to our knowledge the first time reproducible absorption coefficients of less than 50 ppm/cm have been obtained in a repeated manner.

Growth along the c axis tends to demonstrate a lower absorption coefficient than growth along the a-axis. For example, when comparing crystals 191 and 192 in particular we can see the average absorption coefficient goes from 56 ppm/cm to 44 ppm/cm when changing the crystalline direction from a to c-axis, while keeping the other growth parameters identical. The growth along c-axis leading to lower 1064 nm absorption levels is very beneficial to cryogenic GW detectors, as in any case the c-axis is necessary to limit detrimental birefringence effects [18].

It can also be noticed that the first series of four crystals pulled shows a much higher α coefficient than the other ones (taking the 204 and 214 a-axis crystals out), ranging from 56 to 33 ppm/cm with the absorption coefficient being lower after each crystal growth. From this first series, it seems like the higher the rotation speed, the lower the absorption coefficient. It can also be noted that in this first series of crystal growth, the absorption lowered after each growth.

In order to correlate the growth parameters to the absorption coefficients, **figure 4** presents the absorption coefficients α as a function of the rod rotation rate for samples 196 to 199 and 205 to 213. These samples were chosen as they were all grown along the c-axis. When we compare the samples grown with the same rod rotation speed, whatever the pulling rate and

the rotation rate we can see that the sample grown with the counter rotation (crucible rotation) have a higher α absorption coefficient than the ones grown without crucible rotation.

When looking at the pulling rate variations, there does seem to be a reducing of the absorption coefficient with the lowering of the pulling rate, independently of the lowering of the absorption over time in our experiment. In particular, the latest crystals 206, 207 and 212 showed average absorption coefficients of 11 ppm/cm, 11 ppm/cm and 10 ppm/cm respectively. Pulling the crystal at low pulling rate (1mm/hour) does seem to help obtain better behaving crystals architecture in regard to the 1064 nm absorption.

This result was expected as lowering the pulling rate gives more time for the crystallization kinetic and limit stress propagation and dislocation density [25] and allows for better structure regarding lattice relaxation, which could be positive to obtain the lowest absorption.

Finally, the three samples (197,198 and 213) grown with the crucible counter rotation turned on (crucible rotation), show a moderate higher optical absorption (18ppm/cm, 24ppm/cm and 20ppm/cm) compared to similar samples without counter rotation. That indicates that the counter rotation has no beneficial effect regarding the optical absorption. Increasing pulling rate to 2mm/hour and rotation rate >4rpm degrades the absorption coefficient (α>20ppm/cm). Through figure 5, the pulling rate and seed rotation rate affect the absorption coefficient. There is a critical balance between these two parameters and they can compensate each other's.

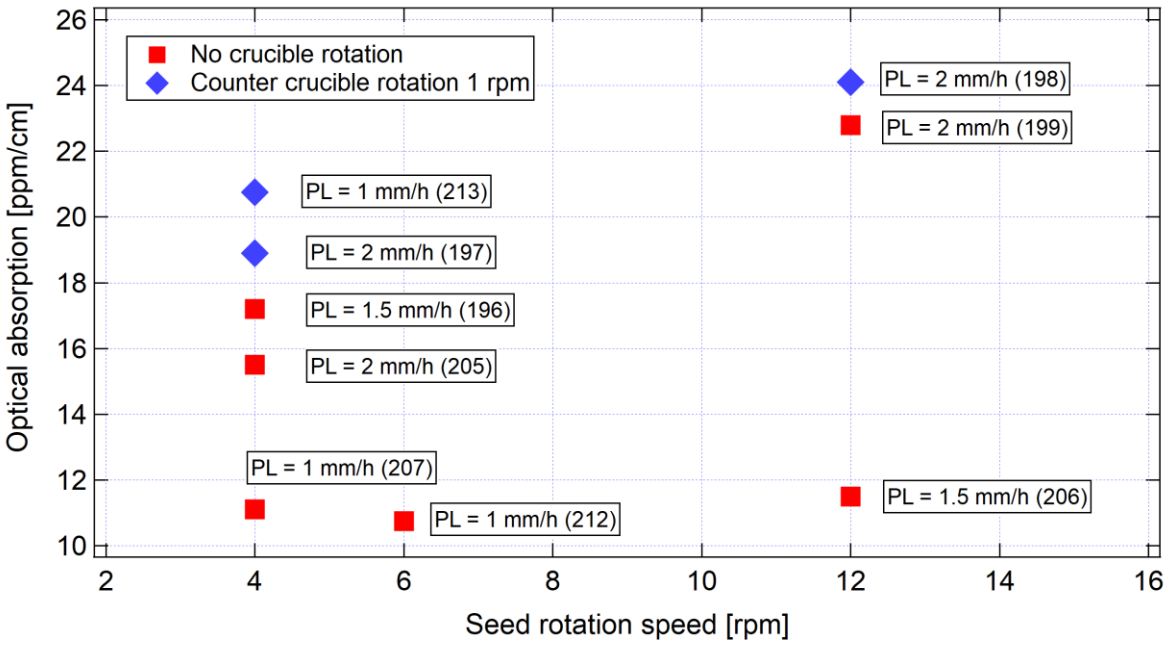

Figure 4. Evolution of the optical absorption coefficient (α) as a function of rotation rate (rpm) and pulling rate (mm/hour)

3.3 Optical absorption uniformity

The absorption mappings of each individual sample give information about the spatial distribution of the optical absorption. **Figure 5** shows the absorption maps of the sapphire single crystals grown under stationary stable regime using the-Czochralski process with the horizontal and vertical axis representing the position in mm and the α absorption coefficient in ppm/cm being displayed by the colour scale. On nearly all the samples, the closer you are

to the edge, the higher the absorption coefficient, with its value doubling between the centre and the edge. This effect is clearly visible in most of the maps in **figure5**.

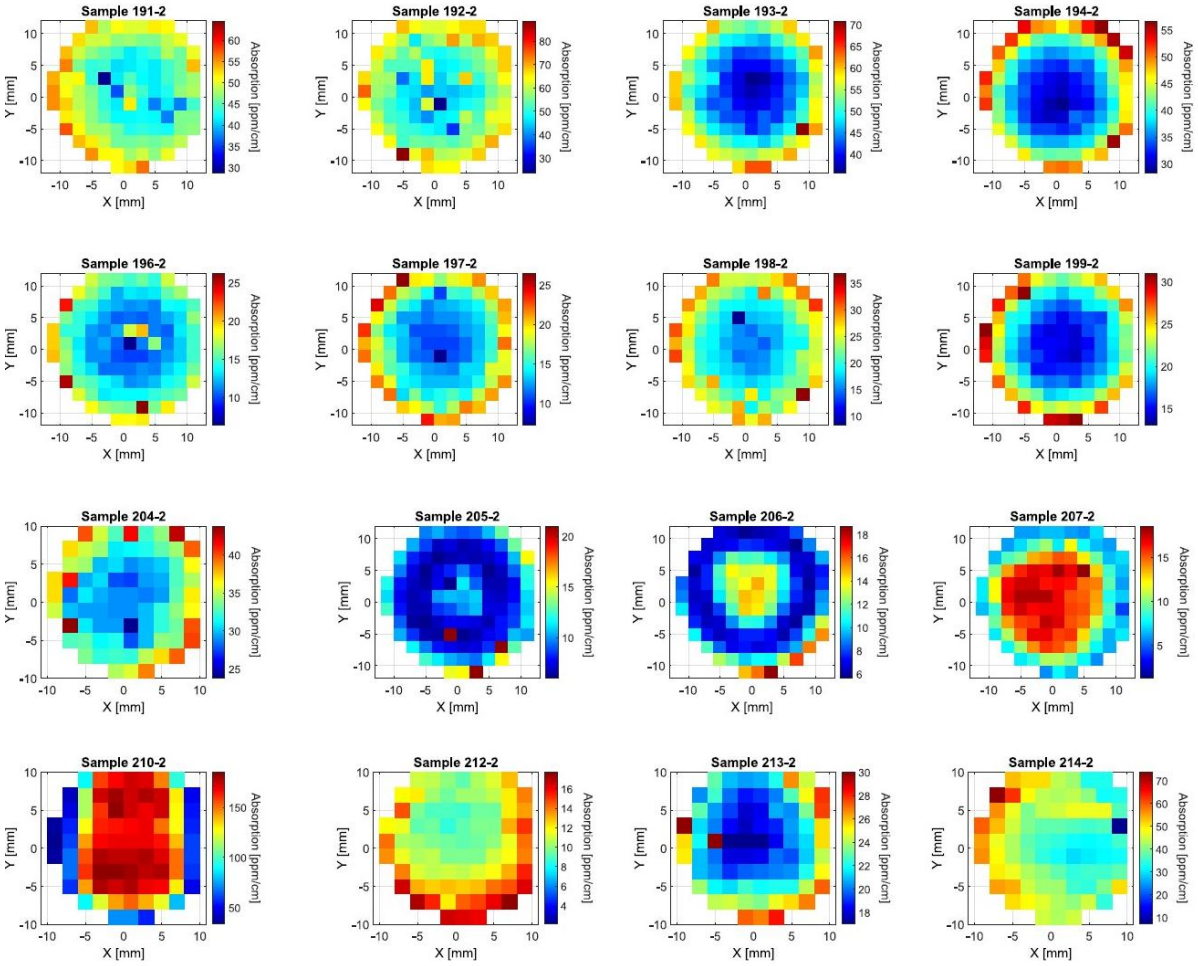

Figure 5. 2D optical absorption maps of sapphire crystal as a function of position and growth parameters.

As each crystal was cut in 3 or 4 samples along the growth axis (**figure 6**), it is also possible to study the evolution of the absorption from head to tail, as presented in **figure 7**. On the majority of crystals, we found that the overall trend is an increase of the absorption as we get closer to the tail. We suppose that this is caused by the lowering of the melt level inside the crucible during growth. This changes the thermal gradients of the melt, leading to higher defects and therefore higher absorptions. The most homogenous samples regarding the absorption are the ones with the lowest pulling rate.

On some samples, a high local absorption point was measured, as we can see in the maps of samples 204-3 and 205-2 in **figure 8**. These absorbing points can vary greatly in intensity as we can see that on sample 204-3 we have an absorption of 400 ppm/cm when the rest of the sample shows values for α under 50 ppm/cm where on sample 205-2 there is a local increase of about 60 ppm/cm, going from 20 ppm/cm in the surrounding points to 80 ppm/cm on the absorption point. The increase is lower on sample 193-4 (close to tail), going from around 30 ppm/cm to 42 ppm/cm on the "absorption point". The cause of these local high absorption defects is not yet understood and their interpretation has to be done carefully.

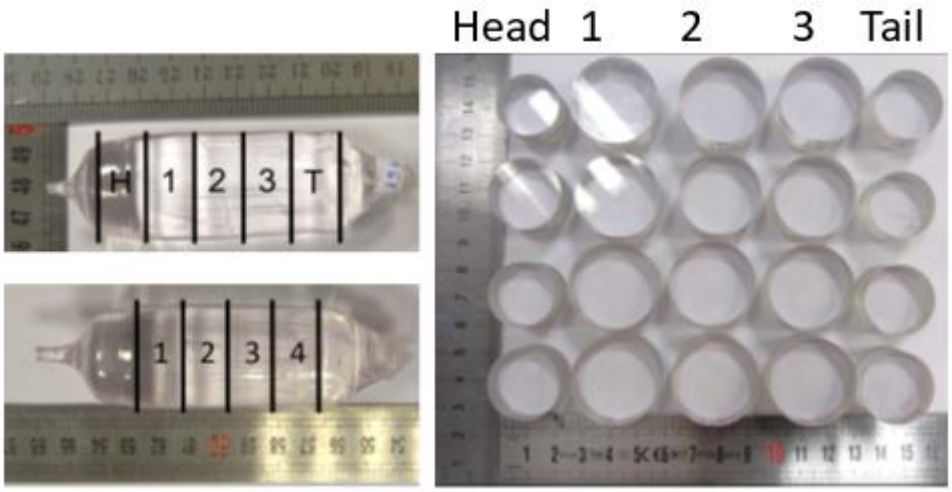

Figure 6. Example of the two different cuts done on our crystals. On the top how the first eight crystals were cut, with 5 samples cut and polished but only the three in the middle being exploitable. H and T stand for Head and Tail respectively. On the bottom, the second cut which yielded 4 usable samples.

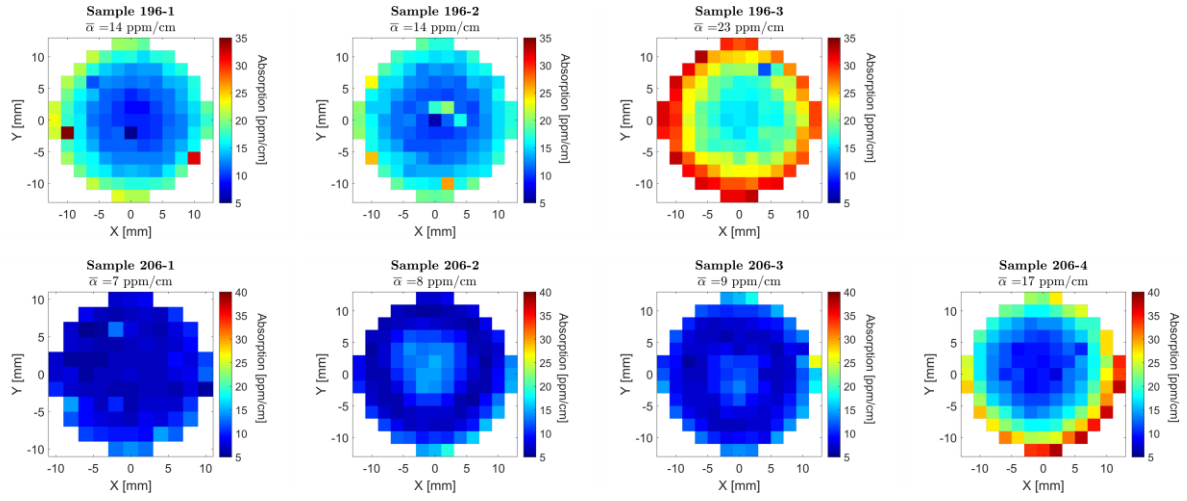

Figure 7. Evolution of the absorption maps along the thickness for two different representative crystals. The colour scale is identical for all samples from the same crystal. From left to right, samples from the head to the tail.

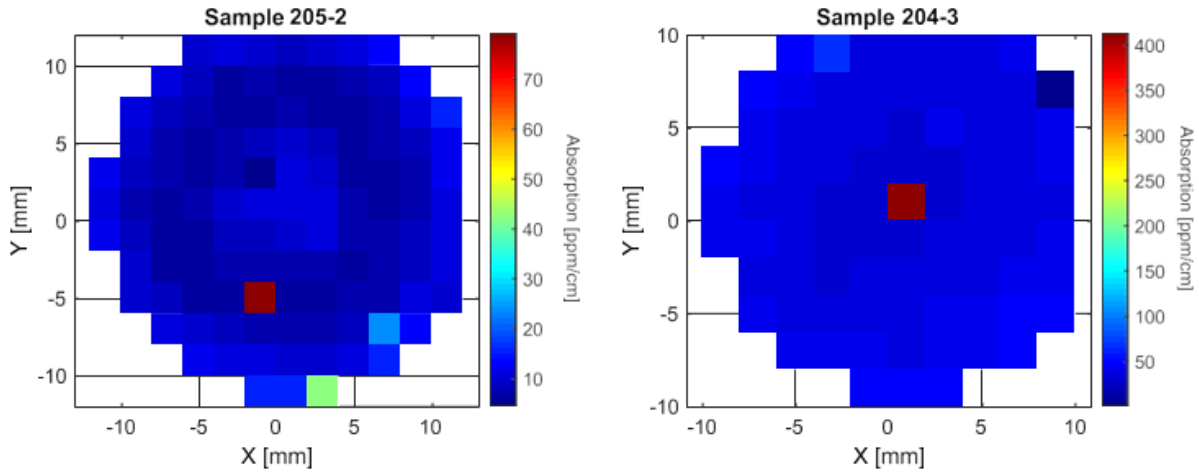

Figure 8: Example of two crystal samples with well-localised points with much higher absorption than the surrounding.

These local absorption points can also be caused by local closest neighbour defect clusters composed of iron or titanium ions in aluminum sites [26].

The optical losses of eight different crystals from 200 to 800nm are plotted in **figure 9a**. We are not aware of any direct correlation in the absorption between the visible and the near-infrared (1064 nm). However, the absorption bands in the visible wavelength give information about the presence of optically active elements and could hint at the culprits behind the 1064 nm absorption. The base line of the losses was offset, as it is not dependant on the samples themselves but rather on several external factors, including the temperature, humidity level, as well as on the polishing and calibration of our apparatus. All our crystals display very similar loss spectra.

In this, **figure 9** two sharp different regions can be seen: the first between 200 and 330nm

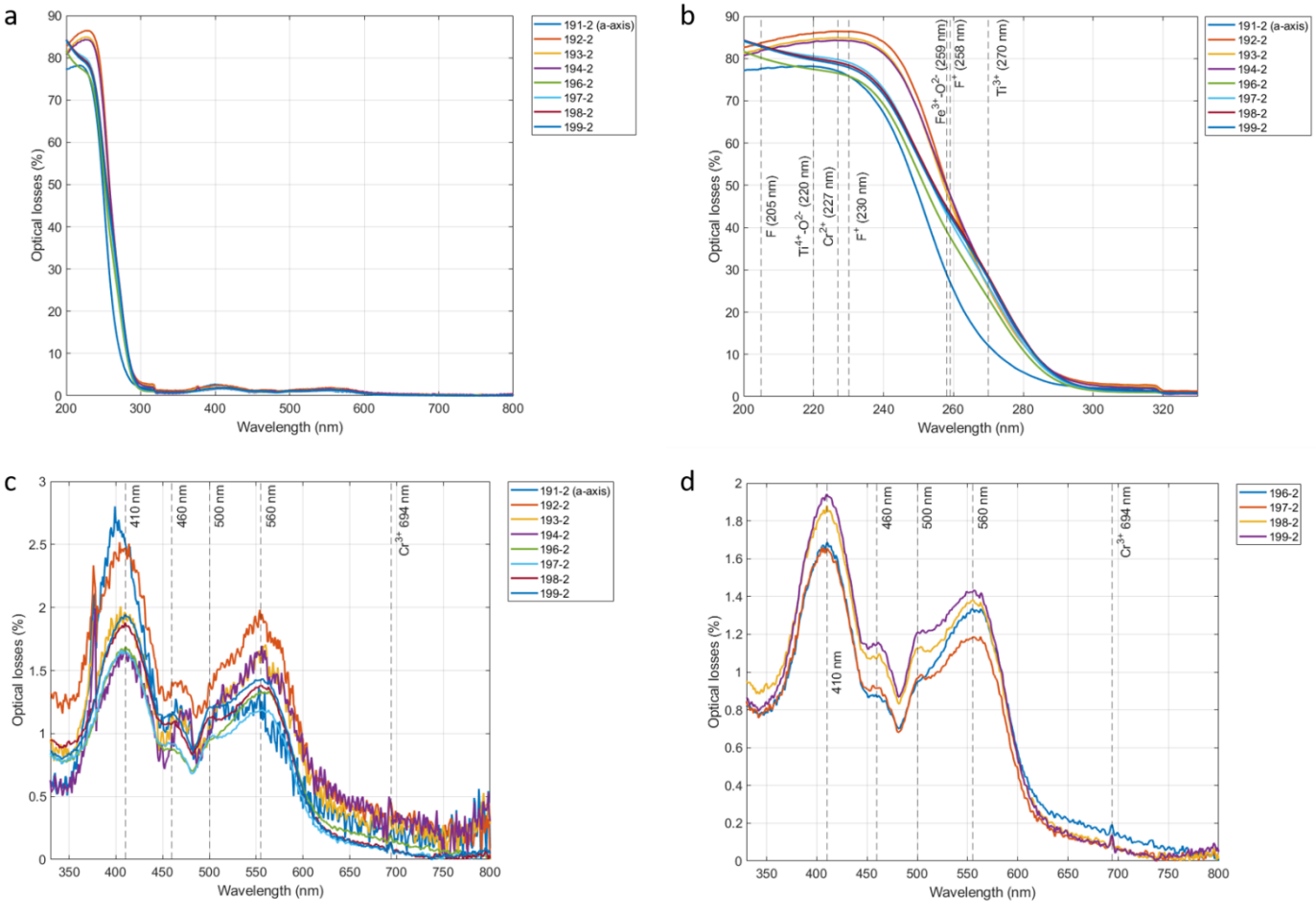

where we measure a very fast increase in the optical losses from the base level of 5 to 10% at 300nm to over 80% at 200 nm. The second region, from 330 to 800nm shows much lower variations that are difficult to see as the spectra is dominated by the first region. For this reason, the spectra were plotted between 200 and 330nm in **figure 9b** and between 330 and 800nm in **figure 9c.**

Figure 9. (a) Optical losses of 8 samples taken from the middle of 8 different crystals measured from 200 to 800nm. (b) Optical losses of the 8 samples measured from 200 to 330nm. (c) Optical losses of the 8 samples measured from 330 to 800nm. (d) Optical losses of 4 samples measured from 330 to 800nm.

In the 330 to 800nm range, the spectra of samples 191-2 to 194-3 have a much lower signal to noise ratio. To allow for an easier identification of the peaks we have also plotted the spectra of only the samples from crystals 4 to 8 in **figure 9d**. At these wavelength, the majority of absorbing defects are caused by the presence of isovalent (Cr^{3+}, Ti^{3+}, Co^{3+}, Ni^{3+}, Fe^{3+}, Mn^{3+}, V^{3+}) transition metal impurities in an aluminium lattice site [27, 28]. In other words, optical absorption in the visible wavelengths are mostly caused by the substitution of an Al^{3+} ion by another 3+ ion. Transition metals in a 3+ ionic state loses their 4s electrons and have incomplete 3d shells. These electrons interact with the surrounding crystal field which results in them having several low energy levels in which optical transitions can occur. These optical transitions leads to absorptions in the visible wavelength and gives colour to the crystal.

This is seen in natural sapphires, where the natural blue colour of sapphires is caused by Fe^{3+} and Ti^{3+} ions and the red colour of ruby by Cr^{3+} [29-34]. When aluminium sites are occupied by divalent ions such as Mg^{2+} or Be^{2+}, their charge is compensated by O^{1-} ions instead of the normal O^{2-} valence state. This O^{1-} ion is called a trap hole and these hole then pair with Cr^{3+} or Fe^{3+} producing a strongly absorbing colour centre giving sapphires a characteristic orange (called padparadscha) and yellow colour respectively [33, 34]. These colour centres only appear in sapphires grown or heat-treated in an oxidising environment and are therefore not expected on our sapphires grown in argon gas atmosphere.

In our undoped sapphires, there is no dominant effect of a particular dopant over all other impurities. This leads to a fit of the absorption spectra containing many Gaussian contributions which will mathematically always produce a satisfying fit regardless of if it has physical meaning or not. It becomes impossible to give any physical sense to the choice of a particular gaussian fit over another. Instead, we have identified 5 bands in particular on our spectra and will try to present the possible multiple contributions to these bands: two large bands centred at 410 and 560 nm, two smaller shoulders at 460 and 500nm and 530nm and one thin peak at 694 nm.

The first broad band from 380 to 450nm and centred at 410nm seems to correspond to the "residual absorption" peak found in Ti-doped sapphires and is attributed to Ti^{3+} by Moulton et al [35]. The exact process that creates this absorption is not known but the intensity of this peak is dependent on the square of the Ti^{3+} concentration in Ti-doped sapphires, indicating the role of Ti^{3+} pairs. Another likely contribution is the transition of a Cr^{3+} 3d electron from $^4A_2$ to $^4T_1$ absorbing at 409nm [28, 33, 36, 37]. Other contributions could come from the second excitation of a 3d electron of V^{3+} absorbing at 401nm [28, 33] or an aluminium vacancy closest neighbour with an OH– defect absorbing at 413nm [38, 39].

As the first band decreases, a small shoulder around 460nm is visible before a sharp decrease at 480 nm. This peak could be caused by two main contributions: the 450nm absorption peak of Fe^{3+}-Fe^{3+} pairs caused by the excitation of one 3d electrons from the ground state to the $^4A_1$ energy level [29, 33, 40, 41, 42], and the absorption caused by a $F^{2+}{}_2$ centre (two F^+ centres closest neighbours) at 455nm [43-45].

The third band is similar to the previous one in the sense that it appears as a small shoulder on top of a larger gaussian peak and is centred around 500 nm. This could correspond to the main absorption of Ti^{3+} doped sapphires used in lasers called the pump band which is a broad absorption peak from 400 to 700nm composed of a high band centred at 490nm and a second low band peaking around 560nm [28, 35, 46]. This two-peaked absorption corresponds to the excitation of a 3d electron of a Ti^{3+} from its ground level $^2T_2$ to its first excited state ^2E which is split in two by the Jahn-Teller effect.

It can be noted that in Ti doped sapphire, the first 490nm peak has a higher intensity than the second 560nm while we observe the opposite on our samples. This supports our hypothesis that in our undoped sapphire this peak has multiple sources. Other such sources can be the 558nm $^4A_2$ to $^4T_1$ transition of Cr^{3+} [28, 37, 47], the first excitation of a 3d electron of V^{3+} at 570nm [28, 47, 48] and the Fe^{2+}-Ti^{4+} closest neighbour pair inter-valence charge transfer at 570nm [27, 31, 40, 47]. While this pair has been attributed the characteristic blue colour of natural sapphire, recent work by X-ray absorption near-edge spectroscopy (XANES) have suggested that this absorption peak is due to a Fe^{3+}-Ti^{4+} mixed acceptor state with two energy levels above the valence band of sapphire [49]. Lastly, the thin band at 694 nm is the Raman activated R_1 and R_2 peak of Cr^{3+} that previously measured [28, 37, 48].

Despite having two possible vanadium peaks in our analysis, the very low concentrations of vanadium found through GDMS reduces the likeliness of these optical centres having a visible contribution to our spectra. As no other coloured centre with an OH^- defect was found in the spectra, we have also ruled out the aluminium vacancy closest neighbour with an OH^- defect absorbing at 413nm from our possible explanations. The 455nm peak of $F^{2+}{}_2$ centre is usually associated with the presence of the 357nm peak of the $F^+{}_2$ centre (one F+ and one F centre closest neighbours) which is not measured in our spectra, reducing the plausibility of this peak.

This leaves only peaks explained by chromium, titanium and iron, which is also correlated to the stronger measured presence of these three elements when compared to the other 3+ transition metals. As mentioned earlier, the measured spectra on our sapphires do not show clear single gaussian peaks, but instead complex absorption bands. These bands are created by the interaction of multiple absorption sources, of varying intensity all contributing to the overall larger band. Taking this into consideration, we attribute the first 410nm peak to a combination of the 409nm Cr^{3+} absorption and the 410nm Ti^{3+} pairs absorption. The small shoulder around 460nm is attributed to the 450nm Fe^{3+} absorption peak, and the 10nm wavelength difference is likely due to the difficulty in identifying the peak centre due to the much more intense 410nm peak. The wavelengths of these peaks can also change by up to 10nm depending on authors, further comforting the choice of attributing Fe^{3+} to this peak. For the same reasons, we attribute the 500nm peak to the first Ti^{3+} split 3d electron transition that produces a broad peak centred at 490 nm. The large peak around 560nm is attributed to both the second Ti^{3+} split 3d electron transition and Cr^{3+} at 560 and 566nm respectively. Lastly, the small peak at 694nm is easily attributed to Cr^{3+}.

All the absorption peaks of both Cr^{3+} and Ti^{3+} ions have been attributed to absorption features in our measured spectra [34, 35], further corroborating the peak assignments. The Fe^{3+} peak attribution is less clear as while the 450nm absorption of Fe^{3+}- Fe^{3+} pairs does seem to be present, the presence of the two other major Fe^{3+} peaks is less evident. These are the 3d

electron excitation of one the two Fe^{3+} ions in a Fe^{3+}- Fe^{3+} pair from the ground $^6A_1$ state to ^4E absorbing around 377nm and the excitation of a single Fe^{3+} 3d electron from $^6A_1$ to $^4T_2$ at 388nm [28, 29, 33, 40, 41, 42]. Fe^{3+} ions have an absorption cross section in the 400 to 700nm range one order of magnitude lower than that of Cr^{3+} or V^{3+} [33, 34]. This means that for the same concentration, the absorption intensity of Fe^{3+} of much lower than Cr^{3+}. The concentrations of these elements in our samples were shown to be between tenths to a couple of ppm by the GDMS analysis (**see table 3**). It is therefore expected that the absorption peaks caused by Fe^{3+} have a lower intensity than the ones caused by Cr^{3+}. This means that the two 377 and 388nm peaks are likely present in our spectra but are hidden by the much more intense combined absorptions of Cr^{3+} and Ti^{3+} pairs at 409nm and 410nm respectively.

The last absorbing defects that could be present in our samples is the Fe^{2+}-Ti^{4+} intervalence charge transfer (or Fe^{3+}-Ti^{4+} mixed acceptor state) which displays two absorption peaks at 580 and 700 nm. While the first peak could be present but hidden in the much more intense peaks of Ti^{3+} and Cr^{3+} around 560 nm, the second peak at 700nm was not detected on our samples, meaning this absorbing defect is either not present in quantities that would create detectable absorptions by our spectrometer. Although this pair has a very high absorption cross section in the 400 to 700nm range one order of magnitude greater than Cr^{3+}, in Czochralski grown sapphires, the Fe^{2+}- Ti^{4+} are largely dissociated due the high growth temperature (2050 °C) and very few pairs exist [33] and thus don't contribute visibly to the absorption of our samples.

The identified colour centres behind each of the peaks of our measured optical losses spectra between 330 and 800nm are summarised and presented in **table 4**.

Table 4: Absorption features in our optical loss spectra and their colour centre attribution

Absorption peak	**Defects**	**Comment**
410 nm	Fe^{3+}-Fe^{3+} : $^6A_1 \rightarrow {}^4E$ (377 nm) Fe^{3+} : $^6A^1 \rightarrow {}^4T^2$ (388 nm) Cr^{3+} : $^4A_2 \rightarrow {}^4T_1$ (409 nm) Ti^{3+}-Ti^{3+} (410 nm)	likely hidden by more intense peaks likely hidden by more intense peaks
460 nm	Fe^{3+}-Fe^{3+} : $^6A^1 \rightarrow {}^4A_1$ (450 nm)	10nm offset
500 nm	Ti^{3+} : $^2T_2 \rightarrow {}^2E_a$ (490 nm)	10nm offset
560 nm	Cr^{3+} : $^4A_2 \rightarrow {}^4T_2$ (558 nm) Ti^{3+} : $^2T^2 \rightarrow {}^2E_b$ (560 nm)	
694 nm	Cr^{3+} : $^4A_2 \rightarrow {}_2E$ (694 nm)	Two peaks at 693 and 694.4nm

Figure 9b presents the optical losses spectra between 200 and 330 nm. As mentioned earlier, the spectra present a very steep increase in optical losses from 5 to 10% at 300nm to over 80% at 220nm in a linear-like fashion, making peak identification complicated.

The sudden decrease in optical losses at 320nm is a measurement artefact due to the change in the lamp used by the spectrometer. In the 200 to 330nm wavelengths, several types of defects can be responsible for optical absorption in sapphires. In particular, F centres type defects, which are one or two electrons trapped in an oxygen vacancy, have several absorption peaks. F^+ centres (one electron trapped in an oxygen vacancy) have three transitions from its base energy level which absorb at 197, 230 and 258 nm.

F centres (two electrons trapped in an oxygen vacancy) have an intense absorption at 205nm [27, 37, 38, 43, 50].

Impurity type defects also have electron transition levels or charge-transfers that cause absorption in this range. As it is difficult to extract specific peaks from the spectra, only the ones caused by our known optically active elements will be presented: titanium, chromium and iron. Studies on titanium-doped sapphires have shown that a charge-transfer process where a O^{2-} exchanges an electron to a Ti^{4+} ion absorbs strongly at 220nm [35, 51, 52]. The charge transfer between O^{2-} and Ti^{3+} absorbs at 180nm [51] and Ti^{3+} ions also have an absorption at 270nm but the exact origin of this absorption does not make consensus [35]. For chromium two peaks can affect the absorption in this region: Cr^{2+} absorbing at 227nm and the inter-valence charge transfer of Cr^{3+}-O^{2-} absorbing at 180nm [39, 51]. In the case of Fe^{3+}, no 3d transition absorb in this wavelength range, but three different Fe^{4+}-O^{2-} charge transfers have been measured at 172, 194 and 259 respectively [33, 51].

These identified possible absorption peaks have been added on **figure 9b** and are referenced in **table 5**. A few peaks below our detection limit of 200nm have also been included as the higher wavelength end of their peak could play a role.

Table 5. Possible absorbing defects in our sapphire samples between 200 and 330nm

Wavelength (nm)	180	180	194	197	205	220	227	230	258	259	270
Defects	Cr^{3+}-O^{2-}	Ti^{3+}-O^{2-}	Fe^{3+}-O^{2-}	F^+	F	Ti^{4+}-O^{2-}	Cr^{2+}	F^+	F^+	Fe^{3+}-O^{2-}	Ti^{3+} pairs

The samples can be separated into three groups when looking at their optical losses spectra in **figure 9b** : group 1 with 191-3 (which is also the only a-axis sample in this group), then group 2 composed of samples 192-3, 193-3 and 194-4 and finally group 3 with samples 196-2, 197-2, 198-2 and 199-2. In the 260 to 300nm wavelengths, all the crystals display a very similar increase in optical losses with the exception of 191-3 which shows a slower increase than the other crystals. The sharp optical losses increase with smaller wavelengths in this sample also seems to be different to the other groups.

In particular, in this sample the very high absorption feature in the lower wavelength is centred closer the Ti^{4+} and Cr^{2+} absorption at 220 and 227 nm than around the F^+ 230nm absorption. This can also be correlated with a lower overall increase in the optical losses on this sample in the 200 to 230nm region, which could indicate a lower F and F^+ concentration in this sample compared to the others.

While the samples in group 2 and 3 show a very similar behaviour in the 265 to 330nm range, the samples in group 3 display a steeper increase in their optical losses. It is not clear whether this steeper increase is a combined effect of the peaks both below (Ti^{4+}, Cr^{2+}, F^+) and above (F^+) or if there is a contribution by a non-identified absorption feature.

Lastly, unlike the other samples which have a small decrease in the optical losses from 220 to 200 nm, the optical loss of the samples in group 3 continues to increase up to 200 nm. This indicates a stronger influence of absorption features under our detection limit of 200nm on these samples compared to the others, such as the 197nm absorption of F+ centres or the 194nm and 180nm absorptions of the charge transfers of Fe^{3+}-O^{2-}, Ti^{3+}-O^{2}– and Cr^{3+}-O^{2-}.

Overall the absorption of our samples in the 200 to 800nm range is caused by both intrinsic defects, in particular F centres caused by oxygen vacancies, and some impurity species,

namely chromium, titanium and iron. It is however difficult to extract quantitative data from these measures as the intensity of each peak not only depends on the concentration of the impurity elements and their respective absorption cross sections, but also on their valence state and on the proximity of other impurity or vacancy defects that could allow for charge transfers.

Comparing the Cr^{3+} emissions of our crystals to other sapphires with absorptions in the thousands of ppm/cm at 1064 nm have shown that our samples contained much more Cr3+ than the higher absorbing crystals. This work is still under progress and will be published later, but this has led us to eliminate chromium as a potential source of absorption at 1064 nm. We have identified two hypotheses on the origin of the optical absorption in sapphire: first an intervalence charge transfer in a face-sharing Fe^{2+} - Fe^{3+} defect clusters which absorb in the 1000-1111 nm range [29, 42, 53]. The second origin pointed toward to the role of Ti^{3+} - Ti^{4+} pairs in this absorption [54] however the more recent work by Moulton et al. [35] seem to show that this absorption is caused independently by both Ti^{3+} pairs and the interaction of Ti^{4+} ions with their associated Al vacancy in complex defect structures.

According to the GDMS (Glow Discharge Mass Spectrometry) results done on 3 crystals, the concentrations of both of these elements (Ti and Fe) are very low with only a few ppm of the total weight. If these defects were distributed uniformly in the bulk, the probability that 2 Titanium or Iron atoms form complex defect clusters would be very low.

4.Conclusions

We have successfully grown different undoped sapphire crystals using different growth parameters. The single crystals were crystallized under stationary stable regime using a and c-axis orientation. Whatever the selected growth parameters, the crystal are free of macroscopic defects such as cracks and inclusions. Through Photo-deflection spectroscopy we have successfully mapped the 1064nm optical absorption of sapphire crystals. In all except one sample, we have obtained sub 50ppm/cm absorption, and even absorption around 10ppm has been registered. This is the first time such low absorption has been reported on sapphire in a controlled and repeated manner. The comparison of the growth parameters with the absorption has given insight on the influence of these parameters and we have shown than c-axis Czochralski grown sapphires display a lower absorption than a-axis one. We have also found that both a low pulling rate and a slow rod rotation speed help reduce the absorption, with the pulling rate being the more important parameter. No beneficial effect of the crucible counter-rotation was found. The optical losses of the sapphire samples from 200 to 800nm have shown that in particular both Cr^{3+} and Ti^{3+} play a major role in the visible absorption of our samples, with Fe^{3+} being less visible but still present. In the shorter wavelengths, these species, as well as F type centers play a role in the high absorption of the sapphires, although the steep increase in optical losses made peak identifying harder. This gives us a first insight on the possible culprits behind the 1064nm absorption of sapphire.

Acknowledgements

The work is supported by the DOSFAP and SEPO450 Projects “AAP Auvergne Rhone Alpe Region”. In the frame of SaphirLab joint project (Thanks to Labcom ANR program), we are grateful for the great help of RSA Le Rubis Company. The authors are thankful to Dr O. Benamara for the experimental help.

References

[1] LIGO Scientific Collaboration and Virgo Collaboration, Physical Review Letters, 2016, **116**, 061102.

[2] P. R. Saulson, Fundamentals of Interferometric Gravitational Wave Detectors, 2nd ed., World Scientific Books, 2017.

[3] P. Binetruy, A. Bohe, C. Caprini, and J. F. Dufaux, Journal of Cosmology and Astroparticle Physics, 2012, **2012**, 027.

[4] V. N. Kurlov, Sapphire: Properties, Growth, and Applications, Encycl. Mater. Sci. Technol, 2001, p. 8259.

[5] V. Pishchik, L. A. Lytvynov and E. R. Dobrovinskaya, Sapphire, Springer US, Boston, MA, 2009.

[6] F. A. Ponce and D. P. Bour, Nature, 1997, 386, 351.

[7] P. F. Moulton, J. Opt. Soc. Am. B, 1986, 3, 125.

[8] Belov, N.V. Structure of Ionic Crystals and Metatallic Phases

[Struktura Ionnykh Kristallov I Metallicheskikh Faz into Russian];

Academy of the Sciences of the USSR: Moscow, Russia, 1947.

[9] Schmid, F, Khattak, C. P. Proc. SPIE 1989, 1112, 25.

[10] C.H. Chen, J.C. Chen, C.W. Lu, C.M. Liu, J. Cryst. Growth., 2011, 318, 162–167.

[11] G.G. Wang, J.C. Han, H.Y. Zhang, M.F. Zhang, H.B. Zuo, Z.H. Hu, X.D. He, Cryst.

Res. Technol., 2009, 44 (9), 995–1000.

[12] V. Chandrasekharan and H. Damany. Birefringence of sapphire, magnesium fluoride, and quartz in the vacuum ultraviolet, and retardation plates. Appl. Opt., 1968, 7(5), 939–941.

[13] Jérôme Degallaix, Chunnong Zhao, Li Juf, and David Blair. Superiority of sapphire over silicon

test masses regarding thermal noise and thermal lensing for laser interferometers with transmissive

optics. Journal of Physics: Conference Series., 2006, 32, 404–412.

[14] QiulingWen, Wei Xinyu, Feng Jiang, Xizhao Lu, and Xipeng Xu. Focused ion beam milling of single crystal sapphire with a-, c-, and m-orientations. Materials, 2020, 13, 2871..

[15] K. Topp and D. Cahill, Zeitschrift für Physik B, 1996, **101**, 235–245.

[16] F. M. Kiessling, P. G. Murray, M. Kinley-Hanlon, I. Buchovska, T. K. Ervik, V. Graham, J. Hough, R. Johnston, M. Pietsch, S. Rowan, et al., Phys. Rev. Research, 2022, **4**, 043043.

[17] E. Hirose, D. Bajuk, G. Billingsley, T. Kajita, B. Kestner, N. Mio, M. Ohashi, B. Reichman, H. Yamamoto, and L. Zhang, Phys. Rev. D, 2014, **89**, 062003.

[18] Y. Michimura, H. Wang, F. Salces-Carcoba, C. Wipf, A. Brooks, K. Arai, and R. X. Adhikari, Phys. Rev. D, 2024, **109**, 022009.

[19] H. Li, E. A. Ghezal, A. Nehari, G. Alombert-Goget, A. Brenier, and K. Lebbou, Optical Materials, 2013, **35**, 1071–1076.

[20] H. Li, E. A. Ghezal, G. Alombert-Goget, G. Breton, J. M. Ingargiola, A. Brenier, and K. Lebbou, Optical Materials, 2014, **37**, 132–138.

[21] G. Alombert-Goget, H. Li, J. Faria, S. Labor, D. Guignier, and K. Lebbou, Optical Materials, 2016, **51**, 1–4.

[22] RSA Le Ruby Company, https://alumine-rsa.com/.

[23] T. Duffar, Crystal growth processes bases on capillarity, Czochralski, Floating zone; Shaping and crucibles techniques, Willey, 2010.

[24] W. B. Jackson, N. M. Amer, A. C. Boccara, and D. Fournier, Applied Optics, 1981, **20**, 1333–1344.

[25] I. Lasloudji, F. Mokhtari, A. Nehari, G. Alombert-Goget, and K. Lebbou, CrystEngComm, 2018, **20**, 1110-1115.

[26] M. R. Phillips, Journal of the American Ceramic Society, 1994, **12**.

[27] V. Pishchik, L. A. Lytvynov, E. R. Dobrovinskaya, Sapphire: Material, Manufacturing, Applications, Springer US, Boston, MA, 2009.

[28] D. S. McClure, The Journal of Chemical Physics, 2004, **36**, 2757–2779.

[29] J. Ferguson and P. Fielding, Australian Journal of Chemistry, 1972, **25**, 1371–1385.

[30] L. V. Nikolskaya, V. M. Terekhova, and M. I. Samoilovich, Physics and Chemistry of Minerals, 1978, **3**, 213–224.

[31] E. Fritsch and G. R. Rossman, Gems & Gemology, 1988, **24**, 3–15.

[32] C. W. Stillwell, The Journal of Physical Chemistry, 2002, **30**, 1441–1466.

[33] E. V. Dubinsky, J. Stone-Sundberg, and J. L. Emmett, Gems & Gemology, 2020, **56**, 1–27.

[34] M. Jeršek, G. Jovanovski, B. Boev, and P. Makreski, ChemTexts, 2021, **7**, 19.

[35] P. F. Moulton, J. G. Cederberg, K. T. Stevens, G. Foundos, M. Koselja, and J. Preclikova, Opt. Mater. Express, 2019, **9**, 2216–2251.

[36] M. E. Innocenzi, R. T. Swimm, M. Bass, R. H. French, A. B. Villaverde, and M. R. Kokta, Journal of Applied Physics - J APPL PHYS, 1990, **67**, 7543–7546.

[37] F. Benabid, et al., Journal of Physics D: Applied Physics, 2000, **33**, 589.

[38] K. H. Lee and J. H. Crawford, Phys. Rev. B, 1977, **15**, 4065–4070.

[39] T. J. Turner and J. H. Crawford, Solid State Communications, 1975, **17**, 167–169.

[40] J. J. Krebs and W. G. Maisch, Phys. Rev. B, 1971, **4**, 757–769.

[41] K. Eigenmann, K. Kurtz, and H. H. Günthard, Chemical Physics Letters, 1972, **13**, 54–57.

[42] A. R. Moon and M. R. Phillips, Journal of the American Ceramic Society, 1994, **77**, 356–367.

[43] B. D. Evans, Journal of Nuclear Materials, 1995, **219**, 202–223.

[44] G. J. Pogatshnik, Y. Chen, and B. D. Evans, IEEE Transactions on Nuclear Science, 1987, **34**, 1709–1712.

[45] Y. Chen, M. M. Abraham, and D. F. Pedraza, Nuclear Instruments and Methods in Physics Research Section B: Beam Interactions with Materials and Atoms, 1991, **59-60**, 1163–1166.

[46] P. F. Moulton, J. Opt. Soc. Am. B, 1986, **3**, 125–133.

[47] R. M. Macfarlane, The Journal of Chemical Physics, 2004, **39**, 3118–3126.

[48] H. Wang, X. Y. Yu, F. Liu, M. Alam, and G. C. Wu, Crystals, 2022, **12**, 4.

[49] P. Wongrawang, N. Monarumit, N. Thammajak, P. Wathanakul, and W. Wongkokua, Materials Research Express, 2016, **3**, 026201.

[50] B. G. Draeger and G. P. Summers, Phys. Rev. B, 1979, **19**, 1172–1177.

[51] H. H. Tippins, Phys. Rev. B, 1970, **1**, 126–135.

[52] W. C. Wong, D. S. McClure, S. A. Basun, and M. R. Kokta, Phys. Rev. B, 1995, **51**, 5682–5692.

[53] S. Sugano, Multiplets of transition-metal ions in crystals, Elsevier, 2012.

[54] R. L. Aggarwal, A. Sanchez, M. M. Stuppi, R. E. Fahey, A. J. Strauss, W. R. Rapoport, and C. P. Khattak, IEEE Journal of Quantum Electronics, 1988, **24**, 1003–1008.